Aranda-Iglesias, D., Vadillo, G. y Rodríguez-Martínez, J.A. (2017). Oscillatory behaviour of compressible hyperelastic shells subjected to dynamic inflation: a numerical study. *Acta Mechanica*, 228(6), pp. 2187–2205.

DOI: https://doi.org/10.1007/s00707-017-1821-8

Oscillatory behaviour of compressible hyperelastic shells subjected to dynamic inflation: a numerical study

D. Aranda-Iglesias · G. Vadillo · J. A. Rodríguez-Martínez

Abstract In this paper, we have investigated the role played by the material compressibility in the oscillatory behaviour of hyperelastic spherical shells subjected to dynamic inflation. For that purpose, we carried out a comprehensive nondimensional numerical analysis using: (i) a finite differences MacCormack's scheme implemented in MATLAB, and (ii) a finite element model developed in ABAQUS/Explicit (Abaqus Explicit v6.10 user's manual, version 6.10 edn. ABAQUS Inc., Richmond, 2010). We have detected that numerical dispersion and diffusion impose limits to the capacity of the computations to describe the shock wave that emanates from the inner surface of the shell due to the application of the inflation pressure. Nevertheless, both numerical approaches capture the essential features that describe the oscillatory behaviour of the shell, including the maximum stretch of the oscillation. Using the key nondimensional groups that control the problem at hand, we have conducted a parametric study to assess the role played by nondimensional applied pressure, material compressibility, and nondimensional shell thickness in the oscillatory behaviour of the specimen. We have shown the interplay between the maximum amplitude of the oscillation and the applied pressure and obtained the critical pressure for which the oscillatory behaviour is lost, leading to an unbounded expansion of the spherical shell. Moreover, our calculations have revealed that the wave propagation within the specimen plays a key role in the dynamic response of the shell. The phase portraits used to represent the oscillatory behaviour of the spherical shell show a characteristic sawtooth form that is accentuated with the increase in material compressibility and shell thickness.

1 Introduction

The first studies dealing with the nonlinear dynamic behaviour of hyperelastic shells are dated in the early 60's. Knowles [18,19] investigated, for the first time, the large-amplitude radial oscillations of very long, thick-walled, cylindrical tubes. Shortly after, Zhong-Heng and Soleki [30] inspected the large-amplitude vibrations of thick-walled spherical shells. In these seminal works, free and forced oscillations with Heaviside step pressure boundary condition were explored. The material was considered incompressible, and the problems were reduced to that of an autonomous motion of a system with a single degree of freedom. The authors provided exact solutions of the trajectory and period of vibrations and paid specific attention to the critical initial and loading conditions that preclude the oscillatory response of the shell. The interest in large-amplitude radial vibrations of hyperelastic incompressible bodies has continued to the present day. A significant number of papers have been published over the last five decades on this specific topic (e.g. [5,6,23,26,28]). For instance, Humphrey and co-workers [10,27] studied the axisymmetric deformations of spherical hyperelastic shells subjected to inner and outer pressure to assess the mechanical (dynamic) stability of intracranial saccular

D. Aranda-Iglesias (✉) · G. Vadillo · J. A. Rodríguez-Martínez
Department of Continuum Mechanics and Structural Analysis, University Carlos III of Madrid,
Avda. de la Universidad, 30, 28911 Leganés, Madrid, Spain
E-mail: faranda@ing.uc3m.es

aneurysms. The axisymmetric dynamic deformations of (dielectric) elastomeric spherical membranes were also investigated by Mockensturm and Goulbourne [22] to assess how these structures could be used as reciprocating and peristaltic pumps. We should also mention the work of Gonçalves et al. [11] who studied the free and forced nonlinear vibrations of pre-stretched hyperelastic membranes subjected to transversal harmonic pressure. The authors developed a single degree-of-freedom model that was verified via comparisons with finite element calculations performed with the code ABAQUS. This work highlighted the influence of the pre-stretching ratio, the strain energy function used to model the material, and the frequency of the applied pressure on the dynamic response of the membrane. Alternatively, Breslavsky et al. [7] proposed a dynamic local model to investigate the nonlinear vibrations of rectangular hyperelastic plates. The model, which allowed to include the *commonly ignored* in-plane displacements to the analysis of bending vibrations of hyperelastic plates [8], was validated with experiments and numerical simulations performed with ABAQUS. The reader is referred to the recent and very detailed review of Alijani and Amabili [2] to obtain further information about the literature published over the last 50 years on the dynamic behaviour of hyperelastic shells.

However, the oscillatory behaviour of compressible hyperelastic shells has received much less attention. Most likely, this is because material compressibility impedes obtaining closed-form solutions of the shell motion. The problem has to be solved numerically. To the authors' knowledge, the first contribution to this field was published by Haddow and Mioduchowski [12]. This work explored the radial oscillations of compressible hyperelastic spherical shells subjected to a step function pressure at their inner surface. Haddow and Mioduchowski [12] showed that the response of compressible and incompressible shells subjected to dynamic inflation is significantly different. For incompressible specimens the effect of the pressure is felt instanta-neously throughout the shell. In the case of compressible spherical shells, the applied pressure leads to the formation of a shock wave, which propagates back and forth, through the thickness of the specimen. In Janele et al. [16], Haddow and co-workers further investigated the radial oscillations of compressible hyperelastic spherical shells. For that, they developed a finite difference model, based on a predictor-corrector scheme, that improved the numerical procedure previously used in Haddow and Mioduchowski [12]. Their attention was focussed on the constitutive sensitivity of the oscillatory behaviour of compressible shells. They used different strain energy functions to model the material behaviour and highlighted the differences between the dynamic response of compressible and incompressible specimens. The phase portraits of compressible shells showed a characteristic sawtooth form (this was not observed for incompressible shells), which revealed the effect of the reflected waves in the oscillatory behaviour of the spherical specimen. Similar results were obtained in Janele et al. [15,17], where Haddow and co-workers investigated the dynamic inflation of compressible cylindrical shells. More recently, we should highlight the work of Antman and Lacarbonara [4], who developed a general approach to the radial motions of compressible nonlinear elastic cylindrical and spherical shells subjected to time-dependent pressure. Using the geometrically exact two-dimensional Cosserat theory developed in [3], the authors pointed out the significant differences in the dynamic response of cylindrical and spherical shells. The reader is referred to Chapter 17 in [3] to obtain additional information about various engineering problems that arise within the context of the dynamic behaviour of nonlinear elastic shells.

The present paper, which complements the aforementioned works [4,12,16], revisits the problem of a compressible spherical shell subjected to constant pressure at its inner surface. The goal is to provide further insights into the role played by the applied pressure, the material compressibility, and the shell thickness in the oscillatory behaviour of the specimen. For that task, we have addressed the problem using two different numerical approaches: (i) a finite differences scheme implemented in MATLAB, and (ii) a finite element model developed in ABAQUS. On the one hand, we have detected that numerical diffusion and dispersion impose limits to the capacity of (these) numerical methods to describe the shock wave that emanates from the inner surface of the shell due to the applied pressure. On the other hand, we have shown that both numerical approaches capture main features of the oscillatory response of the spherical shell, including the maximum amplitude of the oscillations. Using the key nondimensional groups that control the problem at hand, we have conducted a comprehensive parametric analysis and showed, for different specimen thicknesses and degrees of material compressibility, the interplay between the maximum amplitude of the oscillations and the applied pressure. In addition, we have investigated the critical loading conditions and material behaviours (degrees of compressibility) for which the oscillatory behaviour is lost, leading to an unbounded expansion of the spherical shell.

2 Problem formulation

In this section, we formulate the problem of a thick-walled spherical shell subjected to radially symmetric dynamic inflation. The material is taken to be isotropic and compressible within the framework of finite nonlinear elasticity. The main features of the mathematical derivation are presented, while further details can be found in the work of Janele et al. [16].

Let $\{R, \Theta, \Phi\}$ denote the spherical polar coordinates in the reference configuration such that $R_i \leq R \leq R_o$. If the material is deformed so that the spherical symmetry is maintained, the motion is given by:

$$r = r(R, t); \quad \theta = \Theta; \quad \phi = \Phi \tag{1}$$

where $\{r, \theta, \phi\}$ are the spherical polar coordinates in the current configuration such that $r_i \leq r \leq r_o$. Under these conditions, the deformation gradient tensor is given by:

$$\mathbf{F} = \text{diag}\{\lambda_r, \lambda, \lambda\} \tag{2}$$

where the radial stretch is $\lambda_r = \frac{\partial r}{\partial R}$ and the circumferential stretch is $\lambda = \frac{r}{R}$. Moreover, the particle velocity is $v = \frac{\partial r}{\partial t}$, and the first Piola–Kirchoff stress tensor is given by:

$$\mathbf{S} = \text{diag}\{S_r, S_\theta, S_\theta\}. \tag{3}$$

The fundamental equations, formulated in Lagrangian description, which govern the loading process, are given below.

- Kinematic relations:
  - Radial stretch rate

$$\frac{\partial \lambda_r}{\partial t} - \frac{\partial v}{\partial R} = 0; \tag{4}$$

  - Circumferential stretch rate

$$\frac{\partial \lambda}{\partial t} - \frac{v}{R} = 0. \tag{5}$$

    Hereinafter, we indistinctly denote the circumferential stretch rate as $\frac{\partial \lambda}{\partial t}$ or $\dot{\lambda}$.
- Conservation of linear momentum along the radial direction:

$$\rho_0 \frac{\partial v}{\partial t} - \frac{\partial S_r}{\partial R} - \frac{2\,(S_r - S_\theta)}{R} = 0 \tag{6}$$

  where ρ_0 is the initial material density.
- Constitutive equations: In this work our attention is restricted to isothermal loading processes at constant temperatures. Following Ogden [25], we use the *isochoric–volumetric* decomposition of the strain energy function:

$$\psi(\overline{I}_1, \overline{I}_2, J) = \psi_{\text{iso}}(\overline{I}_1, \overline{I}_2) + \psi_{\text{vol}}(J) \tag{7}$$

  where $\overline{I}_1 = J^{-2/3}(\lambda_r^2 + 2\lambda^2)$ and $\overline{I}_2 = J^{-4/3}(2\lambda_r^2\lambda^2 + \lambda^4)$ are the first and second invariants of the isochoric part of the right Cauchy–Green strain tensor and $J = \lambda_r\lambda^2$ is the determinant of the deformation gradient tensor. We have selected the Mooney–Rivlin material model to characterize the isochoric part:

$$\psi_{\text{iso}}(\overline{I}_1, \overline{I}_2) = C_{10}\left(\overline{I}_1 - 3\right) + C_{01}\left(\overline{I}_2 - 3\right) \tag{8}$$

  where C_{10} and C_{01} are material parameters such that $G = 2(C_{10} + C_{01})$ is the initial shear modulus. From Bucchi and Hearn [9] we have taken $C_{10} = 210587.307$ MPa and $C_{01} = 1504.76719$ MPa. These material constants correspond to vulcanized rubber and were originally reported by Treolar [29]. We have selected the expression proposed by Ogden [24] to characterize the volumetric part:

$$\psi_{\text{vol}}(J) = \frac{K}{\beta^2}\left(\beta \ln J + J^{-\beta} - 1\right) \tag{9}$$

  where K is the initial bulk modulus and β is an empirical material parameter. Note that, in the limit of small deformations, $K = \frac{2G(1+\nu)}{3(1-2\nu)}$ where ν is the initial Poisson's ratio. In forthcoming sections of this paper, we will carry out systematic variations of ν in order to explore the role played by the material compressibility in the dynamic response of the spherical shell. Moreover, according to Ogden [24], we have taken $\beta = 9$. Finally, if the strain energy function takes the form $W(\lambda_r, \lambda) = \psi(\overline{I}_1, \overline{I}_2, J)$, the stresses are given by:

– Radial stress

$$S_r = \frac{\partial W}{\partial \lambda_r}; \tag{10}$$

– Circumferential stress

$$S_\theta = \frac{1}{2}\frac{\partial W}{\partial \lambda}. \tag{11}$$

The problem formulation is completed with the following initial and boundary conditions:

$$S_r\,(R,0) = S_\theta\,(R,0) = 0, \qquad v\,(R,0) = 0, \tag{12}$$

$$S_r\,(R_i,t) = -\lambda(R_i,t)^2 P, \qquad S_r\,(R_o,t) = 0 \tag{13}$$

where P is a constant pressure applied in the inner surface of the spherical shell. Note that the relation between the radial Piola–Kirchoff stress and the radial Cauchy stress is $S_r = \lambda^2\sigma_r$. Therefore, the boundary condition in the inner surface of the shell can be alternatively expressed as $\sigma_r\,(R_i,t) = -P$. These relations will be used in Sect. 5 to analyse the stress field in the spherical shell during the loading process.

It is convenient at this point to introduce the following nondimensional set of variables:

$$\hat{R} = \frac{R}{R_i}, \qquad \hat{r} = \frac{r}{R_i}, \qquad \hat{S}_r = \frac{S_r}{C_{10}}, \qquad \hat{S}_\theta = \frac{S_\theta}{C_{10}},$$

$$\hat{t} = \frac{t}{R_i}\sqrt{\frac{C_{10}}{\rho_0}}, \qquad \hat{v} = v\sqrt{\frac{\rho_0}{C_{10}}}, \qquad \hat{W} = \frac{W}{C_{10}}, \qquad \hat{P} = \frac{P}{C_{10}}, \qquad \mu = \left(\frac{R_o}{R_i}\right)^3 - 1 \tag{14}$$

where μ is a nondimensional thickness parameter [18,19] used to represent the geometry of the spherical shell in Sects. 5 and 6. This set of nondimensional variables highlights the dependence of the problem on the geometric and loading parameters μ and $\hat{P}$ that will be systematically varied in Sect. 6. Previous nondimensional variables allow to rewrite the kinematic relations and the balance of linear momentum, Eqs. (4)–(6), as follows:

$$\frac{\partial \lambda_r}{\partial \hat{t}} - \frac{\partial \hat{v}}{\partial \hat{R}} = 0, \tag{15}$$

$$\frac{\partial \lambda}{\partial \hat{t}} - \frac{\hat{v}}{\hat{R}} = 0, \tag{16}$$

$$\frac{\partial \hat{v}}{\partial \hat{t}} - \frac{\partial \hat{S}_r}{\partial \hat{R}} - \frac{2\left(\hat{S}_r - \hat{S}_\theta\right)}{\hat{R}} = 0. \tag{17}$$

The previous system of equations is rearranged in the form:

$$\frac{\partial \mathbf{Q}}{\partial \hat{t}} + \frac{\partial \mathbf{H}\,(\mathbf{Q})}{\partial \hat{R}} + \mathbf{b}\,(\mathbf{Q}) = 0 \tag{18}$$

where $\mathbf{Q} = \left(\lambda_r, \lambda, \hat{v}\right)^{\mathrm{T}}$, $\mathbf{H} = -\left(\hat{v}, 0, \hat{S}_r\right)^{\mathrm{T}}$, and $\mathbf{b} = -\left(0, \frac{\hat{v}}{\hat{R}}, \frac{2\left(\hat{S}_r - \hat{S}_\theta\right)}{\hat{R}}\right)^{\mathrm{T}}$. We can further operate with the previous equations in order to obtain the system in non-conservative form:

$$\frac{\partial \mathbf{Q}}{\partial \hat{t}} - \mathbf{A}\frac{\partial \mathbf{Q}}{\partial \hat{R}} + \mathbf{b}\,(\mathbf{Q}) = 0 \tag{19}$$

where

$$\{\mathbf{A}\} = \begin{Bmatrix} 0 & 0 & -1 \\ 0 & 0 & 0 \\ -\frac{\partial \hat{S}_r}{\partial \lambda_r} & -\frac{\partial \hat{S}_r}{\partial \lambda} & 0 \end{Bmatrix}. \tag{20}$$

The eigenvalues of $\mathbf{A}$, that will be retrieved in Sect. 3, are 0 and $\pm\gamma$, where $\gamma = \sqrt{\frac{\partial^2 \hat{W}}{\partial \lambda_r^2}}$. These are the slopes of three families of characteristics in the $\left\{\hat{R}, \hat{t}\right\}$ plane.

The problem of the dynamic inflation of spherical shells formulated in this section is approached numerically using the methods of finite differences and finite elements. The basic features of the numerical models developed for this purpose are described in Sects. 3 and 4.

3 Finite differences modelling

This section presents the finite differences scheme used to solve the governing equations defined by (18). The scheme is taken from Janele et al. [16], who implemented a modification of MacCormack's predictor-corrector formulation [20] to obtain solutions to problems of shear waves emanating from a cylindrical cavity in an unbounded hyperelastic medium [13,14]. Only the main features of the model are presented here since further details can be found in Janele et al. [16].

In order to construct the numerical solution, we consider a rectangular grid such that $\Pi = \{\hat{R}_j = 1 + j\Delta\hat{R},\ \hat{t}^n = n\Delta\hat{t}\}$, where $j = 0, \ldots, M$ and $n = 0, \ldots, N$. The integration spatial and time steps are $\Delta\hat{R} = \frac{\hat{R}_o - 1}{M}$ and $\Delta\hat{t}$. The forward–backward (predictor–corrector) finite differences relations are, respectively:

$$\mathbf{Q}_j^{\overline{n+1}} = \mathbf{Q}_j^n - \frac{\Delta\hat{t}}{\Delta\hat{R}}\left(\mathbf{H}_{j+1}^n - \mathbf{H}_j^n\right) - \Delta\hat{t}\mathbf{b}_j^n, \tag{21}$$

$$\mathbf{Q}_j^{n+1} = \frac{1}{2}\left\{\mathbf{Q}_j^n + \mathbf{Q}_j^{\overline{n+1}} - \frac{\Delta\hat{t}}{\Delta\hat{R}}\left(\mathbf{H}_j^{\overline{n+1}} - \mathbf{H}_{j-1}^{\overline{n+1}}\right) - \Delta\hat{t}\mathbf{b}_j^{\overline{n+1}}\right\}, \tag{22}$$

where the notation $\mathbf{Q}_j^n = \mathbf{Q}\left(\hat{R}_j, \hat{t}^n\right)$ has been used. The superscript $\overline{n+1}$ refers to predicted quantities.

Application of the finite differences scheme requires boundary conditions for the kinematic variables $\{\lambda_r, \lambda, \hat{v}\}$. However, only the relations $\hat{S}_r\left(R_i, t\right) = -\lambda(R_i, t)^2\hat{P}$ and $\hat{S}_r\left(R_o, t\right) = 0$ are prescribed, which give the relation between λ_r and λ at the inner and outer surfaces of the shell. In order to obtain additional boundary conditions, the finite differences scheme is modified as follows.

- Inner surface of the shell: forward–forward scheme.
  In the predictor step the velocity is computed following the forward scheme used in the general formulation, Eq. (21). The circumferential stretch is obtained using a finite difference form of Eq. (16) taken along the characteristic $\hat{R} = 1$, and the radial stretch is obtained from the prescribed boundary condition, Eq. (13):

$$\hat{v}_0^{\overline{n+1}} = \hat{v}_0^n + \frac{\Delta\hat{t}}{\Delta\hat{R}}\left(\left(\hat{S}_r\right)_1^n - \left(\hat{S}_r\right)_0^n\right) + 2\Delta\hat{t}\left(\left(\hat{S}_r\right)_0^n - \left(\hat{S}_\theta\right)_0^n\right), \tag{23}$$

$$\lambda_0^{\overline{n+1}} = \lambda_0^n + \frac{\Delta\hat{t}}{2}\left(\hat{v}_0^{\overline{n+1}} + \hat{v}_0^n\right), \tag{24}$$

$$\left(\hat{S}_r\right)_0^{\overline{n+1}} = -\left(\lambda_0^{\overline{n+1}}\right)^2\hat{P}. \tag{25}$$

  In the corrector step, we use a similar procedure. However, the backward scheme used in the general formulation for the velocity, Eq. (22), is replaced by a forward scheme.

$$\hat{v}_0^{n+1} = \frac{1}{2}\left\{\hat{v}_0^n + \hat{v}_0^{\overline{n+1}} + \frac{\Delta\hat{t}}{\Delta\hat{R}}\left(\left(\hat{S}_r\right)_1^{\overline{n+1}} - \left(\hat{S}_r\right)_0^{\overline{n+1}}\right) + 2\Delta\hat{t}\left(\left(\hat{S}_r\right)_0^{\overline{n+1}} - \left(\hat{S}_\theta\right)_0^{\overline{n+1}}\right)\right\}, \tag{26}$$

$$\lambda_0^{n+1} = \lambda_0^n + \frac{\Delta\hat{t}}{2}\left(\hat{v}_0^{n+1} + \hat{v}_0^n\right), \tag{27}$$

$$\left(\hat{S}_r\right)_0^{n+1} = -\left(\lambda_0^{n+1}\right)^2\hat{P}. \tag{28}$$

- Outer surface of the shell: backward–backward scheme.
  In the predictor step, the forward scheme used in the general formulation for the velocity, Eq. (21), is replaced by a backward scheme. The circumferential stretch is obtained using a finite difference form of Eq. (16) taken along the characteristic $\hat{R} = \hat{R}_o$, and the radial stretch is obtained from the prescribed boundary condition, Eq. (13),

$$\hat{v}_M^{\overline{n+1}} = \hat{v}_M^n + \frac{\Delta\hat{t}}{\Delta\hat{R}}\left(\left(\hat{S}_r\right)_M^n - \left(\hat{S}_r\right)_{M-1}^n\right) + \frac{2\Delta\hat{t}}{\hat{R}_o}\left(\left(\hat{S}_r\right)_M^n - \left(\hat{S}_\theta\right)_M^n\right), \tag{29}$$

$$\lambda_M^{\overline{n+1}} = \lambda_M^n + \frac{\Delta\hat{t}}{2\hat{R}_o}\left(\hat{v}_M^{\overline{n+1}} + \hat{v}_M^n\right), \tag{30}$$

$$\left(\hat{S}_r\right)_M^{\overline{n+1}} = 0. \tag{31}$$

  In the corrector step we use a similar procedure. The backward scheme used in the general formulation for the velocity, Eq. (22), is used,

$$\hat{v}_M^{n+1} = \frac{1}{2}\left\{\hat{v}_M^n + \hat{v}_M^{\overline{n+1}} + \frac{\Delta\hat{t}}{\Delta\hat{R}}\left(\left(\hat{S}_r\right)_M^{\overline{n+1}} - \left(\hat{S}_r\right)_{M-1}^{\overline{n+1}}\right) + \frac{2\Delta\hat{t}}{\hat{R}_o}\left(\left(\hat{S}_r\right)_M^{\overline{n+1}} - \left(\hat{S}_\theta\right)_M^{\overline{n+1}}\right)\right\}, \tag{32}$$

$$\lambda_M^{n+1} = \lambda_M^n + \frac{\Delta\hat{t}}{2\hat{R}_o}\left(\hat{v}_M^{n+1} + \hat{v}_M^n\right), \tag{33}$$

$$\left(\hat{S}_r\right)_M^{n+1} = 0. \tag{34}$$

To the authors' knowledge, there is no analysis available to determine the stability condition for the scheme (21)–(22). Nevertheless, following Haddow et al. [13], we have investigated the stability of the linear system ($\mathbf{b} = 0$) using the Von-Neumann analysis. In this case, it is required that the Courant number $\xi = \gamma\Delta\hat{t}/\Delta\hat{R} \leq 1$, where γ is the numerically largest eigenvalue of $\mathbf{A}$. We have used this condition in all our calculations, and no numerical instability was encountered (see Sects. 5 and 6). Note that γ defines the propagation speed of radial waves in the shell. The nonlinearity of the material behaviour leads to continuous variations of γ during the loading process, and, consequently, $\Delta\hat{t}$ is adjusted at each time step in order to maintain the same value of ξ with constant $\Delta\hat{R}$. We have selected $\xi = 0.99$, which minimizes numerical diffusion and dispersion [21], and $\Delta\hat{R} = 0.001$ for all the simulations presented in Sects. 5 and 6. Further details are given in Appendix "Finite differences modelling".

It is apparent that the finite differences approach provides flexibility and control over the formulation and resolution of the problem. As such, it is suited to explore the physical phenomena that control the dynamic response of the shell (see Sect. 5).

4 Finite elements modelling

This section describes the features of the axisymmetric finite element model developed to simulate the dynamic inflation of spherical hyperelastic shells. The numerical analyses are carried out using the finite element software ABAQUS/Explicit [1]. The strain energy function presented in Sect. 2 has been implemented into the finite element code by a user subroutine. Consistent with Sect. 2, the problem setting is of a spherical shell with inner and outer radii $\hat{R}_i = 1$ and $\hat{R}_o$ (we will perform variations of the shell thickness), respectively (Fig. 1). The solid is initially at rest and unstretched, while a constant internal pressure $\hat{P}$ is applied at the cavity wall.

The model has been meshed using four node axisymmetric reduced integration elements, CAX4R in ABAQUS notation. The mesh shows radial symmetry in an attempt to retain the symmetry of the problem and reduce the interference of the mesh in the calculations, see Fig. 1. The elements size is constant along the circumferential direction, whereas it increases along the radial direction. Thus, we have ensured that the elements aspect ratio is close to 1:1 within the whole domain. According to Zukas and Scheffer [31], such an element shape is optimal for describing dynamic events that involve large gradients of stress and strain. We have placed 200 elements along the circumferential direction, i.e. the size of the elements located beside the inner perimeter is 0.005×0.005. A mesh convergence study has been performed, and phase plane diagrams (stretch rate

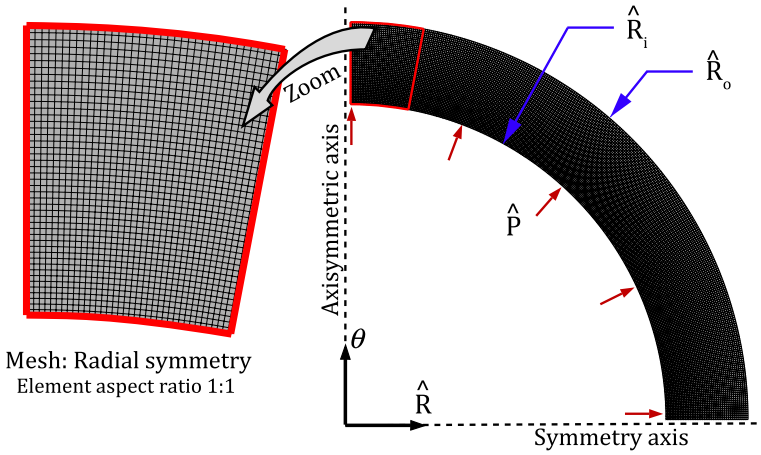

Fig. 1 Finite element mesh and mechanical boundary conditions of the spherical shell, modelled as an axisymmetric solid

versus stretch) were compared against a measure of mesh density until the results converged satisfactorily, see "Appendix 1". Note that ABAQUS/Explicit introduces artificial damping in the calculations in order to attenuate the numerical solution and ensure stability. The code generates bulk viscosity pressures, which are linear and quadratic, respectively, in the volumetric strain rate. This artificial viscosity, which introduces numerical diffusion, is controlled by two parameters ϖ (linear viscosity) and χ (quadratic viscosity). In the calculations shown in Sects. 5 and 6, we have selected the default values of the code 0.06 and 1.2, respectively. Nevertheless, in "Appendix 1" we provide details on the role played by the artificial viscosity in the finite elements results.

In comparison with the finite differences simulations, ABAQUS/Explicit calculations are computationally less costly (markedly). For this reason, the finite element model is especially suited to develop parametric analyses that involve a large number of calculations (see Sect. 6).

In the next sections of the paper, we present selected results obtained from the finite differences and finite elements models. Note that very high levels of compressibility are investigated in a range that exceeds the typical values corresponding to rubber-like materials. Nevertheless, exploring highly compressible solids is justified for the sake of better understanding the essential phenomena involved in the dynamic response of compressible hyperelastic shells. The following analysis is composed of two parts. Firstly we focus on the intervention of stress waves within the specimen, paying specific attention to the role played by the wave propagation phenomena in the dynamic response of the shell. Secondly, we carry out a systematic variation of (nondimensional) applied pressure, material compressibility, and (nondimensional) specimen thickness and analyse the influence of these loading, material, and geometric parameters in the oscillatory response of the spherical shell. Throughout the analysis, a comparison between finite differences and finite elements results is conducted. Additional comparisons are carried out with the analytical solution derived by Zhong-Heng and Soleki [30] for the incompressible solid. This solution is developed in "Appendix 2".

5 Salient features

In this section, we present and discuss some critical outcomes obtained from the numerical models presented in previous sections. Figure 2 shows phase diagrams, $\dot{\lambda}_i$ versus λ_i, obtained using finite differences and finite elements simulations. The applied pressure is $\hat{P} = 0.2$, the thickness parameter is $\mu = 1$, and the initial Poisson's, ratio is $\nu = 0.45$. From this point on, this combination of loading case, geometric condition, and material behaviour will be referred to as the reference case. The phase diagrams show closed orbits, i.e. the dynamic response of the spherical shell is oscillatory. Figure 2a depicts the orbit corresponding to the first oscillation and Fig. 2b to the third oscillation. Both numerical schemes yield phase plane curves with sawtooth form. This is caused by the reflection of stress waves at the shell boundaries. Note that the sawtooth form of the orbits is attenuated with time. This nonphysical behaviour is due to numerical diffusion. The attenuation is

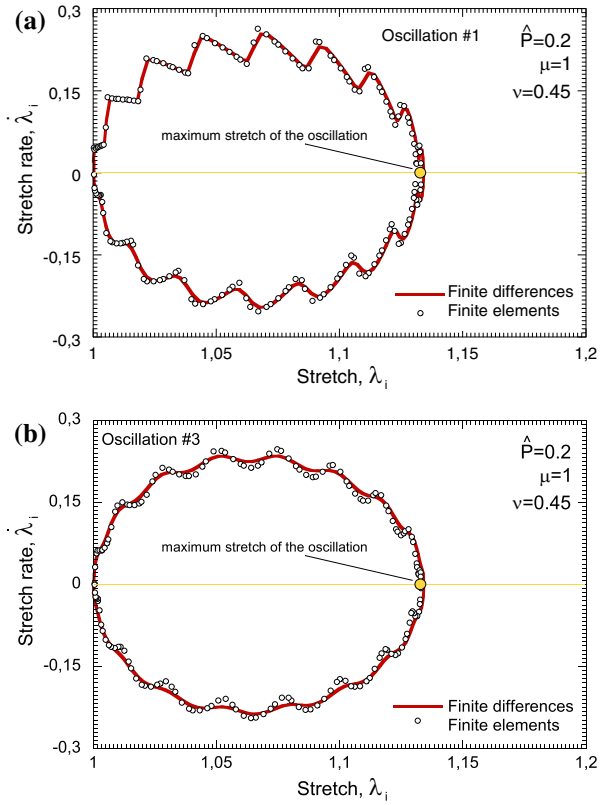

Fig. 2 Comparison between finite differences and finite elements. Phase diagrams, $\dot{\lambda}_i$ versus λ_i. Reference loading case, geometric condition and material behaviour: applied pressure $\hat{P} = 0.2$, thickness parameter $\mu = 1$ and initial Poisson's ratio $\nu = 0.45$. **a** Oscillation #1 and **b** oscillation #3

faster in the case of the finite difference model. Moreover, there is an offset between the finite differences and the finite elements results, which increases with the loading time. This phenomenon is most likely attributed to numerical dispersion. Note that these numerical errors (diffusion and dispersion) barely affect the maximum stretch of the oscillation, which is $\sim$1.13 for both numerical approaches used.

Figure 3 shows the Cauchy radial stress $\hat{\sigma}_R$ and the radial velocity $\hat{v}$ versus the normalized thickness coordinate $\hat{H}$ for the reference loading, geometric, and material configurations. The loading time $\hat{t} = 0.0243$ is such that the front wave that emanates from the inner surface of the shell has not yet reached the outer boundary. A comparison between finite differences and finite elements is shown. The agreement between the results obtained from both numerical codes is remarkable. Starting from the inner surface of the shell, we observe that the radial stress $\hat{\sigma}_R$ and the velocity $\hat{v}$ show a slight (roughly linear) decrease with the normalized thickness coordinate $\hat{H}$. Approaching $\hat{H} \approx 0.4$ we find a sudden drop in $\hat{\sigma}_R$ and $\hat{v}$, which corresponds to the wave front. The drastic variation in the field variables is caused by the compressibility of the solid. This is evidenced in Fig. 4 by the abrupt change in material density observed at the front wave. Nevertheless, the shock is not described as a discontinuity in the calculations because the numerical diffusion smears the wave front across the mesh. Note that the smearing of the shock is more pronounced in the case of the finite differences scheme. Moreover, the finite elements computations show wiggles just behind the shock, which illustrate the numerical dispersion of the finite elements results.

It is apparent that dispersive and diffusive effects limit the capacity of both numerical models to describe the shock wave propagation and the sawtooth form of the phase diagrams over extended periods of time. This limitation is especially relevant in the case of the finite differences scheme. In "Appendix 1" we provide further details on the role played by numerical dispersion and diffusion in the finite differences and finite elements results. Nevertheless, for short loading times, both numerical approaches capture the main physical features that control the oscillatory behaviour of the shell, including the maximum stretch of the oscillation. For the first oscillation, the phase diagram predicted by the finite differences and the finite ele-

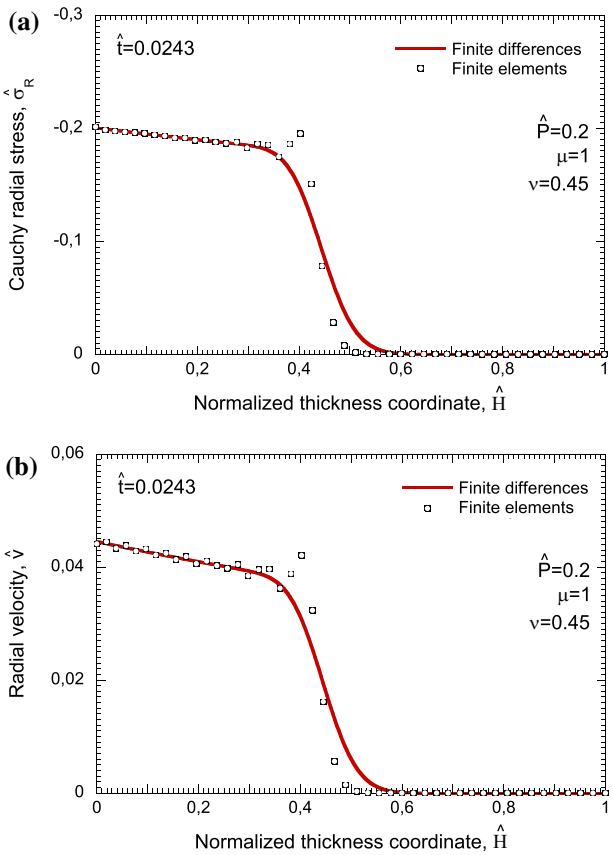

Fig. 3 Comparison between finite differences and finite elements. Reference loading case, geometric condition, and material behaviour: applied pressure $\hat{P} = 0.2$, thickness parameter $\mu = 1$, and initial Poisson's ratio $\nu = 0.45$. **a** Cauchy radial stress $\hat{\sigma}_R$ and **b** radial velocity $\hat{v}$ versus the normalized thickness coordinate $\hat{H} = \frac{\lambda\hat{R}-\lambda_i}{\lambda_o\hat{R}_o-\lambda_i}$ for $\hat{t} = 0.0243$

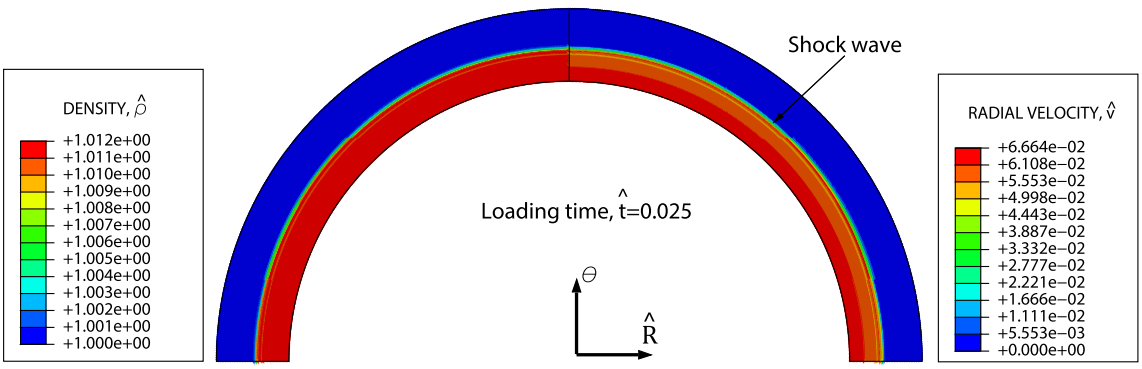

Fig. 4 Finite elements. Reference loading case, geometric condition and material behaviour: applied pressure $\hat{P} = 0.2$, thickness parameter $\mu = 1$ and initial Poisson ratio $\nu = 0.45$. Contours of **a** material density $\hat{\rho}$ and **b** radial velocity $\hat{v}$ for $\hat{t} = 0.0243$

ments is very similar. Thus, relying on the numerical results obtained for the first orbit, in the next section of this paper, we develop a parametric analysis to show the roles played by (nondimensional) applied pressure, material compressibility, and (nondimensional) shell thickness in the oscillatory behaviour of the spherical shell.

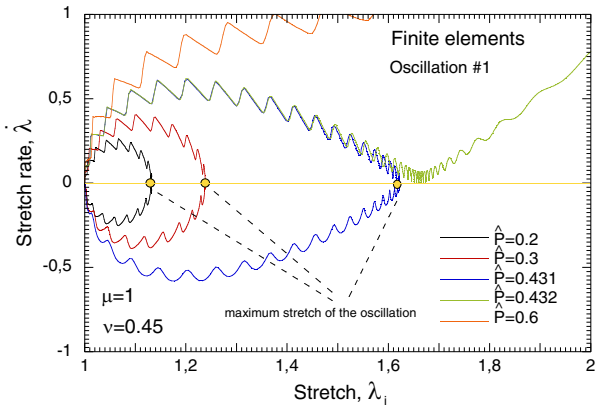

Fig. 5 Finite elements. Phase diagrams, $\dot{\lambda}_i$ versus λ_i. Oscillation #1. Reference geometric condition and material behaviour: thickness parameter $\mu = 1$ and initial Poisson's ratio $\nu = 0.45$. Several loading cases are considered: $\hat{P} = 0.2$, $\hat{P} = 0.3$, $\hat{P} = 0.431$, $\hat{P} = 0.432$ and $\hat{P} = 0.6$

6 Parametric analysis

6.1 The role played by the applied pressure

The aim of this section is twofold: (i) to show the interplay between the maximum amplitude of the oscillation and the applied pressure, and (ii) to determine the limit imposed by the applied pressure to the oscillatory motion of the shell. The reference thickness parameter $\mu = 1$ and initial Poisson's ratio $\nu = 0.45$ are considered in all the calculations presented below.

Figure 5 shows phase diagrams obtained using ABAQUS/Explicit for different values of the applied pressure: $\hat{P} = 0.2$, $\hat{P} = 0.3$, $\hat{P} = 0.431$, $\hat{P} = 0.432$, and $\hat{P} = 0.6$. For the applied pressures $\hat{P} = 0.2$, $\hat{P} = 0.3$, and $\hat{P} = 0.431$ the phase portrait is a closed orbit, i.e. the shell shows an oscillatory motion. Note that, as the pressure increases, the shape of the orbit becomes sharpened. For $\hat{P} = 0.432$ and $\hat{P} = 0.6$ the phase diagram is not closed, i.e. the shell undergoes an unbounded expansion. As anticipated, the applied pressure imposes limits to the oscillatory behaviour of the shell. Note the differences between the phase portraits corresponding to $\hat{P} = 0.432$ and $\hat{P} = 0.6$. For $\hat{P} = 0.6$ the stretch rate is an increasing function of the stretch. On the contrary, for $\hat{P} = 0.432$ the stretch rate first increases until reaching a relative maximum, then decreases up to a point that $\dot{\lambda}$ comes close to zero (if $\dot{\lambda}$ reaches 0 an homoclinic orbit is obtained), and finally increases unbounded.

Figure 6 shows the applied pressure $\hat{P}$ versus the maximum stretch of the oscillation $\lambda_i|_{\dot{\lambda}_i=0}$. A comparison between finite differences and finite elements results is conducted. The agreement between both numerical procedures is remarkable. The amplitude of the oscillation increases with the applied pressure. The $\hat{P} - \lambda_i|_{\dot{\lambda}_i=0}$ curve shows a power-type concave-down shape that extends up to $\lambda_i|_{\dot{\lambda}_i=0} \approx 1.663$. This value of the maximum stretch is reached for $\hat{P} \approx 0.431$ (pressure corresponding to the homoclinic orbit). Larger values of applied pressure lead to the unbounded expansion of the shell (see the open orbits for $\hat{P} \approx 0.432$ and $\hat{P} \approx 0.6$ in Fig. 6).

6.2 The role played by the material compressibility

In this section we explore the role played by material compressibility in the dynamic response of the spherical shell. For that purpose, we have carried out ABAQUS/Explicit calculations using initial Poisson's ratios within the range $0.05 \leq \nu < 0.5$. For the sake of brevity we do not show finite difference results. Nevertheless, we have checked that finite elements and finite differences show very good agreement. Recall that the results for the incompressible case ($\nu = 0.5$) are obtained from the analytical solution developed in "Appendix 2". The reference thickness parameter $\mu = 1$ is considered in all the calculations presented below.

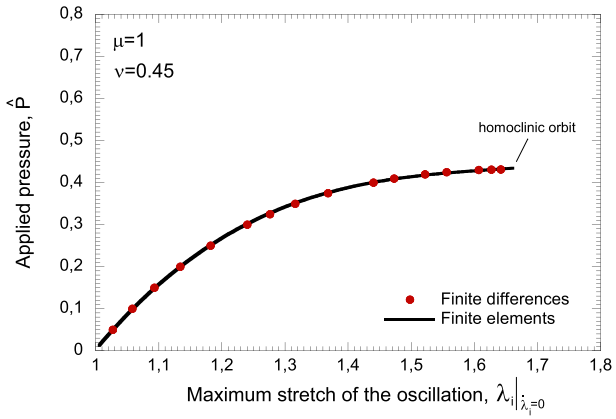

Fig. 6 Comparison between finite differences and finite elements. Applied pressure $\hat{P}$ versus maximum stretch of the oscillation $\lambda_i|_{\dot{\lambda}_i=0}$. Reference geometric condition and material behaviour: thickness parameter $\mu = 1$ and initial Poisson's ratio $\nu = 0.45$

Figure 7 shows phase diagrams obtained using ABAQUS/Explicit for different Poisson's ratios and two different applied pressures: $\hat{P} = 0.2$ in Fig. 7a and $\hat{P} = 0.3$ in Fig. 7b. The sawtooth form of the phase diagram is accentuated with the material compressibility. The role of stress waves propagation in the dynamic response of the shell increases with the decrease in the initial Poisson's ratio. Moreover, at the incompressible limit, the effect of pressure at the inner surface of the shell is felt instantaneously at all radii (no wave propagation), and the phase portrait does not show sawtooth form.

- For $\hat{P} = 0.2$ (Fig. 7a) we have explored 8 different values of the Poisson's ratio: 0.29, 0.3, 0.35, 0.4, 0.45, 0.475, 0.495 and 0.5. For $\nu = 0.29$ the shell expands unbounded, as illustrated by the open orbit of the phase diagram. For Poisson's ratios $\nu \geq 0.3$ the phase diagram is a closed orbit, as corresponds to an oscillatory response of the shell. For a given applied pressure, the degree of compressibility of the material determines whether or not the shell shows an oscillatory response. Moreover, as ν increases, the maximum stretch of the oscillation decreases. For $\nu = 0.495$, the phase orbit virtually overlaps with the one obtained for the incompressible case, and the sawtooth form of the phase diagram is practically negligible.
- For $\hat{P} = 0.3$ (Fig. 7b) we have investigated 7 different values of the Poisson's ratio: 0.35, 0.38, 0.4, 0.45, 0.475, 0.495, and 0.5. For $\nu = 0.35$ and $\nu = 0.38$ the open orbits of the phase diagram indicate that the shell expands unbounded. For Poisson's ratios $\nu \geq 0.4$ the response of the shell is oscillatory. It becomes apparent that, as $\hat{P}$ increases, the loss of the oscillatory behaviour of the shell occurs for largest values of ν. Moreover, as in the case of $\hat{P} = 0.2$, for $\nu = 0.495$, the phase diagram can hardly be distinguished from the one corresponding to the incompressible case.

Figure 8 shows the applied pressure $\hat{P}$ versus the maximum stretch of the oscillation $\lambda_i|_{\dot{\lambda}_i=0}$ for various Poisson's ratios $\nu = 0.1$, $\nu = 0.2$ $\nu = 0.3$, $\nu = 0.35$, $\nu = 0.4$, $\nu = 0.45$, and $\nu = 0.5$ (analytical solution). For each value of ν, the end of the curve indicates that an homoclinic orbit has been reached (see Sect. 6.1). Irrespective of the Poisson's ratio, the $\hat{P} - \lambda_i|_{\dot{\lambda}_i=0}$ curve shows a power-type concave-down shape. As the value of ν increases, the $\hat{P} - \lambda_i|_{\dot{\lambda}_i=0}$ curve is shifted upwards. The pressure required to reach a given value of $\lambda_i|_{\dot{\lambda}_i=0}$ increases with the Poisson's ratio. On the other hand, we observe that the maximum value of $\lambda_i|_{\dot{\lambda}_i=0}$, which corresponds to the homoclinic orbit, strongly decreases with the material compressibility.

This is further illustrated in Fig. 9 where the applied pressure corresponding to the homoclinic orbit $\hat{P}_h$ is plotted as a function of the Poisson's ratio ν. The $\hat{P}_h - \nu$ curve shows a power-type concave-up shape with a slope that increases as the Poisson's ratio approaches incompressibility. While very low values of the Poisson's ratio are explored (up to 0.05), for the sake of providing insights into the effect of compressibility on the dynamic response of the shell, we must recall that such values are not representative of rubber-like materials and may not be within the range for which Eq. (9) was derived and validated.

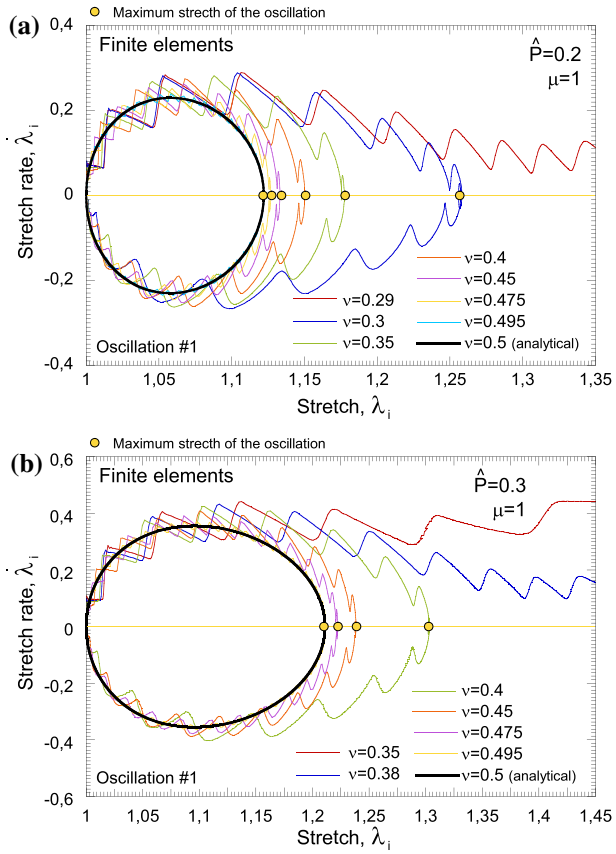

Fig. 7 Finite elements. Phase diagrams, $\dot{\lambda}_i$ versus λ_i. Oscillation #1. Reference geometric condition: thickness parameter $\mu = 1$. Several initial Poisson's ratios ranging from $\nu = 0.29$ to $\nu = 0.5$ (analytical solution) are considered. Two applied pressures are investigated: $\hat{P} = 0.2$ in **a** and $\hat{P} = 0.3$ in **b** (for interpretation of the colours coding of this figure, the reader is referred to the web version of this article)

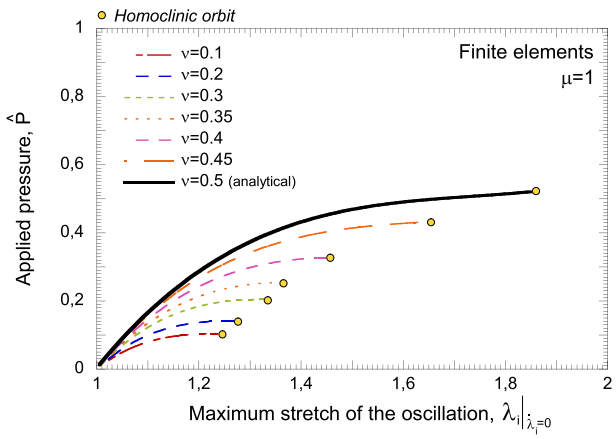

Fig. 8 Finite elements. Applied pressure $\hat{P}$ versus maximum stretch of the oscillation $\lambda_i|_{\dot{\lambda}_i=0}$. Reference geometric condition: thickness parameter $\mu = 1$. Several initial Poisson's ratios are considered: $\nu = 0.1$, $\nu = 0.2$, $\nu = 0.3$, $\nu = 0.35$, $\nu = 0.4$, $\nu = 0.45$, and $\nu = 0.5$ (analytical solution)

6.3 The role played by the shell thickness

In this section, we assess the role played by the thickness in the dynamic response of the spherical shell. For that purpose, we have carried out finite elements calculations using thickness parameters which range from

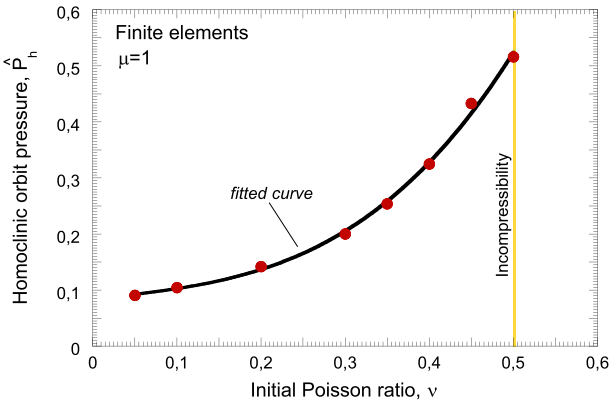

Fig. 9 Finite elements. Homoclinic orbit pressure $\hat{P}_h$ versus initial Poisson ratio ν. Reference geometric condition: thickness parameter $\mu = 1$

$\mu = 1$ to $\mu = 25$. The reference applied pressure $\hat{P} = 0.2$ is considered. The finite element simulations obtained using $\nu = 0.45$ are compared with the analytical solution developed for $\nu = 0.5$. While finite differences results are not shown for the sake of brevity, we have checked that they are in agreement with the finite elements calculations.

Figure 10 shows phase diagrams obtained for $\mu = 5$, $\mu = 10$, and $\mu = 25$. We observe that, as the shell thickness increases, the phase plane orbit becomes gradually reduced: the oscillation is slower and shows smaller amplitude. As the thickness increases, the orbit corresponding to the compressible case looks *less and less* like the ellipse described by the incompressible limit. For $\nu = 0.45$ the number of reflections that occur during the oscillation of the shell decreases as the thickness increases. However, their effect in the shape of the phase portrait is more significant. It is apparent that the role of compressibility in the dynamic response of the spherical shells becomes more important as the thickness increases.

7 Summary and conclusions

In this paper we have explored the role played by the material compressibility in the oscillatory behaviour of spherical shells. The specimens have been subjected to a constant inflation pressure step. The compressible Mooney–Rivlin strain energy function has been used to model the material behaviour. The investigation has been based on a two-pronged numerical approach: (i) we have implemented a finite differences model in MATLAB, and (ii) we have developed a finite elements model in ABAQUS/Explicit.

We have shown that numerical dispersion and diffusion impose limits to the capacity of the finite differences and finite elements models to describe the shock wave that emanates from the inner surface of the shell due to the application of the inflation pressure. Nevertheless, both numerical approaches capture the essential features that describe the oscillatory behaviour of the shell, including the maximum stretch of the oscillation. A key point of our methodology is that finite differences and finite elements models show complementary characteristics. The finite differences scheme provides flexibility and control over the formulation and resolution of the problem. As such, it allowed to uncover the physical phenomena that play a critical role in the dynamic response of the specimens. On the other hand, the finite element model shows significantly lower computational cost. As such, it allowed to develop a comprehensive parametric analysis that showed distinctive features of the oscillatory behaviour of compressible shells. The systematic comparison and analysis of the finite differences and finite elements results led to the following conclusions:

- The maximum amplitude of the oscillation increases with the applied pressure.
- There is a critical pressure, which defines a critical oscillation amplitude, for which the oscillatory behaviour of the shell is lost, leading to an unbounded expansion of the specimen.
- The critical pressure and the critical oscillation amplitude are strongly dependent on the material compressibility.
- The phase portraits used to represent the oscillatory behaviour of compressible shells show a sawtooth form caused by the stress waves intervention within the specimen.

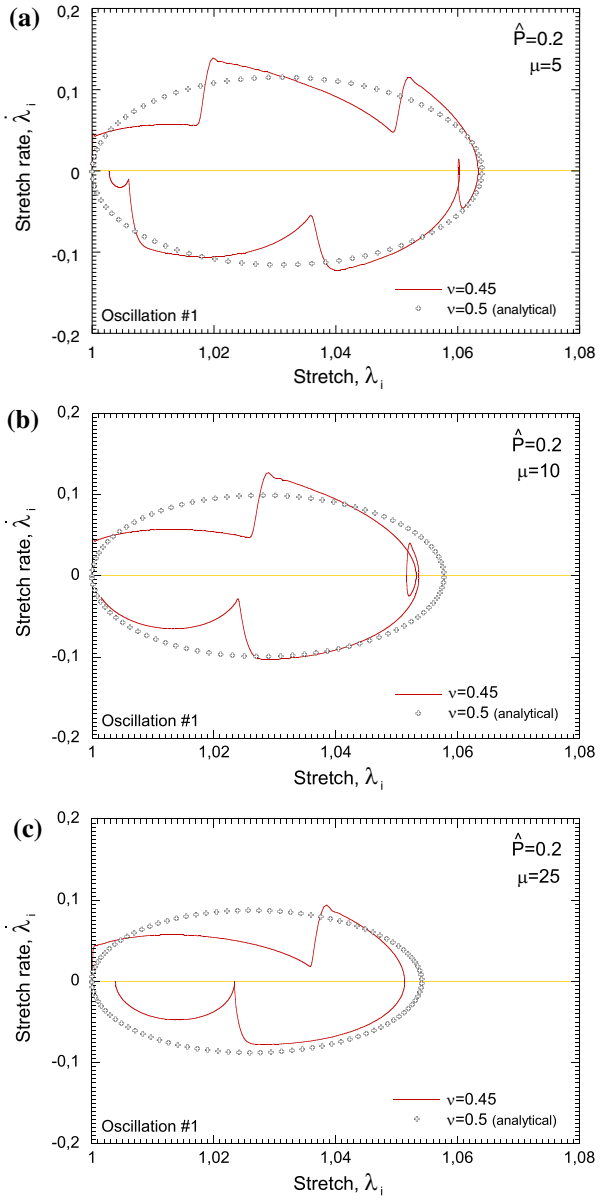

Fig. 10 Phase diagrams, $\dot{\lambda}_i$ versus λ_i. Oscillation #1. Reference loading case: applied pressure $\hat{P} = 0.2$. Three thickness parameters are considered: $\mu = 5$, $\mu = 10$, and $\mu = 25$. Results are shown for two different initial Poisson's ratios: $\nu = 0.45$ (finite elements) and $\nu = 0.5$ (analytical solution)

– The sawtooth form of the phase portraits is accentuated as the material compressibility and shell thickness increase.
– As the specimen thickness increases, the oscillation of the shell is slower and shows smaller amplitude.

All in all, we have developed an exhaustive numerical analysis that moves forward the seminal investigations of Haddow and co-workers [12,16] and provides new insights into the oscillatory behaviour of compressible hyperelastic spherical shells subjected to dynamic inflation.

Acknowledgements The authors are indebted to the *Ministerio de Economía y Competitividad de España* (Projects EUIN2015-62556 and DPI2014-57989-P) for the financial support which permitted to conduct this work.

Appendix 1: Numerical discretization analysis

In this appendix we analyse the convergence of the finite differences and finite element calculations. We focus our attention on the effect that numerical dispersion and diffusion have on the first oscillation of the spherical shell. We have also checked the spurious role of numerical discretization in the front wave description. Nevertheless, those results are not shown here for the sake of brevity. The reference applied pressure $\hat{P} = 0.2$, thickness parameter $\mu = 1$, and initial Poisson's ratio $\nu = 0.45$ are considered in all the examples shown below.

Finite differences modelling

Figure 11 shows phase diagrams for various spatial steps: $\Delta\hat{R} = 0.001$ (reference), $\Delta\hat{R} = 0.002$, and $\Delta\hat{R} = 0.005$. The Courant number is $\xi = 0.99$. We observe that the spatial step plays a key role in the finite difference results. The coarser mesh ($\Delta\hat{R} = 0.005$) *virtually removes* the sawtooth form from the phase diagram. It is apparent that large spatial steps increase numerical diffusion, leading to poor characterization of the wave propagation phenomena within the sample. On the other hand, the difference in the results obtained from $\Delta\hat{R} = 0.001$ and $\Delta\hat{R} = 0.002$ is only detected at the end of the orbit (to be read clockwise) when $\Delta\hat{R} = 0.002$ leads to smoother fluctuations of the stretch rate than $\Delta\hat{R} = 0.001$. Also note that, for $\dot{\lambda} < 0$, there is a slight offset between the results of $\Delta\hat{R} = 0.001$ and $\Delta\hat{R} = 0.002$, which reveals that the increase in the spatial step boosts numerical dispersion.

Figure 12 shows phase diagrams for various Courant numbers: $\xi = 0.99$ (reference), $\xi = 0.9$, and $\xi = 0.8$. All the Courant numbers assessed are smaller than 1 since numerical instability is encountered when $\xi \geq 1$. The spatial step is $\Delta\hat{R} = 0.001$. We do not observe significant differences in the results obtained using different Courant numbers. Note that, as the Courant number increases, the time step increases (see Sect. 3), which reduces the computational cost of the calculations. Moreover, in order to minimize numerical dispersion it is desirable to choose a value of ξ as close to 1 as possible [16,21].

Finite elements modelling

Figure 13 shows phase diagrams for various mesh densities. The size of the elements located in the inner surface of the shell is 0.05×0.05 for mesh 1, 0.01×0.01 for mesh 2 and 0.005×0.005 for mesh 3 (reference). We observe that the maximum stretch of the oscillation and the fluctuations in the stretch rate caused by the intervention of stress waves within the sample are strongly influenced by the element size. As anticipated for the finite differences scheme, numerical dispersion and diffusion increase with the spatial step. The coarser mesh size leads to a significant reduction in the amplitude of the oscillation and predicts a smooth orbit that,

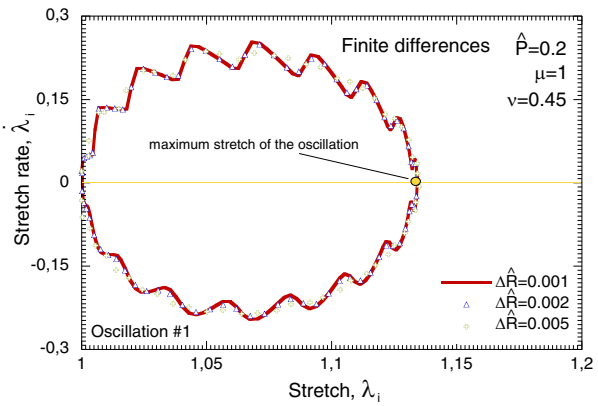

Fig. 11 Finite differences. Phase diagrams, $\dot{\lambda}_i$ versus λ_i. Oscillation #1. Reference loading case, geometric condition and material behaviour: applied pressure $\hat{P} = 0.2$, thickness parameter $\mu = 1$, and initial Poisson's ratio $\nu = 0.45$. Calculations using different spatial steps are shown: $\Delta\hat{R} = 0.001$ (reference), $\Delta\hat{R} = 0.002$, and $\Delta\hat{R} = 0.005$

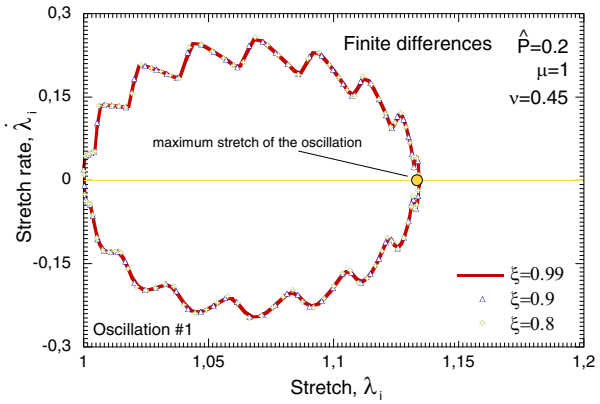

Fig. 12 Finite differences. Phase diagrams, $\dot{\lambda}_i$ versus λ_i. Oscillation #1. Reference loading case, geometric condition, and material behaviour: applied pressure $\hat{P} = 0.2$, thickness parameter $\mu = 1$, and initial Poisson's ratio $\nu = 0.45$. Calculations using different Courant numbers are shown: $\xi = 0.99$ (reference), $\xi = 0.9$ and $\xi = 0.8$

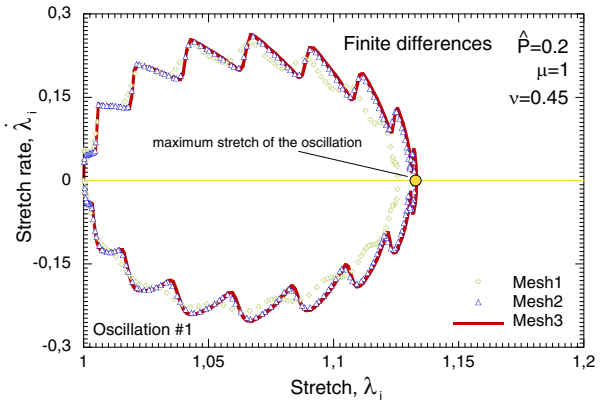

Fig. 13 Finite elements. Phase diagrams, $\dot{\lambda}_i$ versus λ_i. Oscillation #1. Reference loading case, geometric condition and material behaviour: applied pressure $\hat{P} = 0.2$, thickness parameter $\mu = 1$, and initial Poisson's ratio $\nu = 0.45$. Calculations using different mesh sizes: mesh 1 = elements size 0.05×0.05, mesh 2 = elements size 0.01×0.01, and mesh 3 = elements size 0.005×0.005 (reference)

for $\dot{\lambda} < 0$, *barely* reveals the effect of the wave propagation phenomena in the dynamic response of the shell. On the contrary, meshes 2 and 3 show orbits with much sharper profiles, which capture more accurately the wave propagation within the specimen. In addition, there is an offset between the results obtained with the coarser mesh and those corresponding to meshes 2 and 3. The difference in the results obtained from meshes 2 and 3 is small and can be detected only at the end of the orbit (to be read clockwise) when mesh 2 provides (slightly) smoother fluctuations of the stretch rate than mesh 3. The latter has been selected to carry out all the finite element calculations shown in Sects. 5 and 6.

Figure 14 shows phase diagrams for three different linear bulk viscosity parameters: $\varpi = 0.006$, $\varpi = 0.06$ (reference), and $\varpi = 0.6$. We observe that the linear viscosity introduced by the code has significant influence in the phase portrait. Increasing ϖ damps the sawtooth form of the phase diagram. The linear bulk viscosity introduces significant numerical diffusion in the calculations. For the largest value considered ($\varpi = 0.6$), the orbit barely shows traces of wave propagation for $\dot{\lambda} < 0$.

Figure 15 shows phase portraits for three different quadratic bulk viscosity parameters: $\chi = 0.12$, $\chi = 1.2$ (reference), and $\chi = 12$. Unlike what we observed for the linear viscosity parameter, the quadratic one does not have significant influence in the phase diagrams. The differences between the orbits corresponding to $\chi = 0.12$, $\chi = 1.2$, and $\chi = 12$ are negligible.

As anticipated in Sect. 4, in the calculations of Sects. 5 and 6 we have used the default values of ABAQUS/Explicit. On the one hand, we acknowledge that the bulk viscosity is the source of the numerical diffusion in the calculations. On the other hand, we have checked that the linear and quadratic viscosity

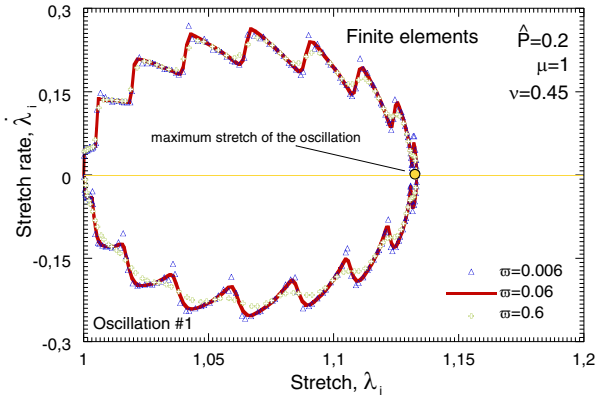

Fig. 14 Finite elements. Phase diagrams, $\dot{\lambda}_i$ versus λ_i. Oscillation #1. Reference loading case, geometric condition, and material behaviour: applied pressure $\hat{P} = 0.2$, thickness parameter $\mu = 1$, and initial Poisson's ratio $\nu = 0.45$. Calculations using different linear bulk viscosity parameters: $\varpi = 0.006$, $\varpi = 0.06$ (reference), and $\varpi = 0.6$

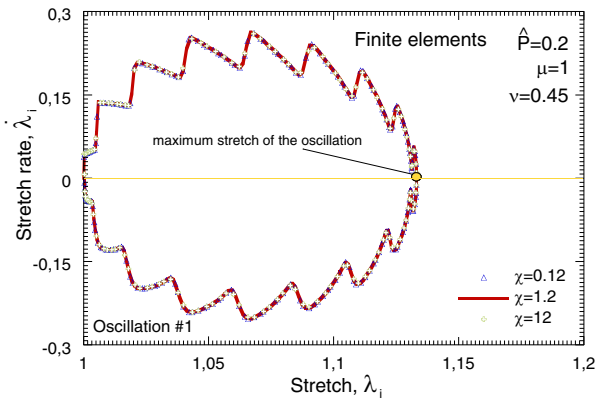

Fig. 15 Finite elements. Phase diagrams, $\dot{\lambda}_i$ versus λ_i. The oscillation #1 is shown. Reference loading case, geometric condition and material behaviour: applied pressure $\hat{P} = 0.2$, thickness parameter $\mu = 1$ and initial Poisson's ratio $\nu = 0.45$. Calculations using different quadratic bulk viscosity parameters: $\chi = 0.12$, $\chi = 1.2$ (reference), and $\chi = 12$

parameters cannot be significantly decreased from their default values since this causes numerical dispersion and stability-related problems.

Appendix 2: Analytical solution for the incompressible solid

In this appendix we solve analytically the dynamic inflation of incompressible spherical shells. The main features of the mathematical derivation are presented, while further details can be found in the work of Zhong-Heng and Soleki [30].

The incompressibility constraint ($\lambda^2\lambda_r = J = 1$) allows to express the circumferential stretch as:

$$\lambda(\hat{R}, \hat{t}) = \left(1 + \frac{\lambda_i(\hat{t})^3 - 1}{\hat{R}^3}\right)^{1/3}. \tag{35}$$

The previous expression shows that the motion of every material point along the thickness is determined if λ_i is known.

Taking the derivative of Eq. (35) with respect to $\hat{R}$, and using the incompressibility condition, the following relation is obtained:

$$\frac{\partial\lambda}{\partial\hat{R}} = -\frac{\lambda^3 - 1}{\hat{R}\lambda^2}. \tag{36}$$

Taking the second derivative of Eq. (35) with respect to nondimensional time, and using the incompressibility condition, we obtain the relation between λ and $\ddot{\lambda}$:

$$\ddot{\lambda} = \frac{\lambda^3 - 1}{\lambda_i^3 - 1}\left[\frac{2\lambda_i \dot{\lambda_i}^2 + \lambda_i^2 \ddot{\lambda_i}}{\lambda^2} - \frac{2\,\lambda_i^4 \dot{\lambda_i}^2}{\lambda_i^3 - 1}\frac{\lambda^3 - 1}{\lambda^5}\right]. \tag{37}$$

These last two relations allow to rewrite the balance of linear momentum, Eq. (17), as follows:

$$\frac{\partial \hat{S}_r}{\partial \lambda} - 2\frac{\hat{S}_r - \hat{S}_\theta}{\lambda - \lambda^{-2}} = -\frac{2\lambda_i \dot{\lambda_i}^2 + \lambda_i^2 \ddot{\lambda_i}}{(\lambda_i^3 - 1)^{1/3}}(\lambda^3 - 1)^{-2/3} + \frac{2\,\lambda_i^4 \dot{\lambda_i}^2}{(\lambda_i^3 - 1)^{4/3}}\frac{(\lambda^3 - 1)^{1/3}}{\lambda^3}. \tag{38}$$

Furthermore, for an incompressible spherical shell, we have that (see, e.g. Ogden [25]):

$$\hat{S}_\theta - \lambda^{-3}\hat{S}_r = \frac{1}{2}\frac{\hat{W}}{\mathrm{d}\lambda}(\lambda) \tag{39}$$

where the nondimensional strain energy function $\hat{W}(\lambda)$ is a sole function of λ. Note that, in the incompressible case, the strain energy function takes the form of Eq. (8).

Thus, integration of Eq. (38) using the boundary conditions defined in Eq. (13) leads to:

$$\hat{P}(\hat{t}) = \int_{\lambda_o}^{\lambda_i} \frac{\hat{W}(\lambda)}{\lambda^3 - 1}\,\mathrm{d}\lambda + \left(1 - \frac{\lambda_i}{(\lambda_i^3 + \mu)^{1/3}}\right)\lambda_i \ddot{\lambda}_i + \left(\frac{3}{2} + \frac{\lambda_i^4}{2(\lambda_i^3 + \mu)^{4/3}} - \frac{2\lambda_i}{(\lambda_i^3 + \mu)^{1/3}}\right)\dot{\lambda}_i^2 \tag{40}$$

where the outer stretch is given by $\lambda_o = \left(\frac{\lambda_i^3 - 1}{\mu + 1} + 1\right)^{1/3}$. The first term in the right hand side of Eq. (40) accounts for the equilibrium straining of the solid, while the two following terms represent the inertial effects. After some manipulation, Eq. (40) is written as:

$$\frac{\mathrm{d}}{\mathrm{d}\lambda_i}\left[\left(1 - \frac{\lambda_i}{(\lambda_i^3 + \mu)^{1/3}}\right)\lambda_i^3 \dot{\lambda}_i^2\right] = 2\lambda_i^2 \hat{P} - 2\lambda_i^2 \int_{\lambda_o}^{\lambda_i} \frac{\hat{W}(\lambda)}{\lambda^3 - 1}\,\mathrm{d}\lambda. \tag{41}$$

The equation above can be integrated to obtain the balance of mechanical energy of the system:

$$\left(1 - \frac{\lambda_i}{(\lambda_i^3 + \mu)^{1/3}}\right)\lambda_i^3 \dot{\lambda}_i^2 + \int_1^{\lambda_i} 2\lambda_i^2 \int_{\lambda_o}^{\lambda_i} \frac{\hat{W}(\lambda)}{\lambda^3 - 1}\,\mathrm{d}\lambda - \frac{2}{3}\hat{P}(\lambda_i^3 - 1) = 0 \tag{42}$$

where the first term defines the kinetic energy of the system, the second term holds for the strain energy stored in the system, and the third one for the work done by the external forces (the applied pressure $\hat{P}$).

The previous expression allows to obtain the relation between $\dot{\lambda}_i$ and λ_i used to calculate the analytical results for the incompressible solid presented in this paper,

$$\dot{\lambda}_i = \sqrt{\frac{\frac{2}{3}\hat{P}(\lambda_i^3 - 1) - \int_1^{\lambda_i} 2\lambda_i^2 \int_{\lambda_o}^{\lambda_i} \frac{\hat{W}(\lambda)}{\lambda^3 - 1}\,\mathrm{d}\lambda}{\left(1 - \frac{\lambda_i}{(\lambda_i^3 + \mu)^{1/3}}\right)\lambda_i^3}}. \tag{43}$$

References

1. ABAQUS/Explicit: Abaqus Explicit v6.10 User's Manual, Version 6.10 edn. ABAQUS Inc., Richmond (2010)
2. Alijani, F., Amabili, M.: Non-linear vibrations of shells: a literature review from 2003 to 2013. Int. J. Non-Linear Mech. **58**, 233–257 (2014)
3. Antman, S.S.: Nonlinear Problems of Elasticity, 2nd edn. Springer, Berlin (2005)
4. Antman, S.S., Lacarbonara, W.: Forced radial motions of nonlinearly viscoelastic shells. J. Elast. **96**, 155–190 (2009)
5. Balakrishnan, B., Shahinpoor, M.: Finite amplitude oscillations of a hyperelastic spherical cavity. Int. J. Non-Linear Mech. **13**, 171–176 (1978)

6. Beatty, M.F.: On the radial oscillations of incompressible, isotropic, elastic and limited elastic thick-walled tubes. Int. J. Non-Linear Mech. **42**, 283–297 (2007)
7. Breslavsky, I.D., Amabili, M., Legrand, M.: Nonlinear vibrations of thin hyperelastic plates. J. Sound Vib. **327**, 4668–4681 (2014)
8. Breslavsky, I.D., Amabili, M., Legrand, M.: Physically and geometrically non-linear vibrations of thin rectangular plates. Int. J. Non-Linear Mech. **58**, 30–40 (2014)
9. Bucchi, A., Hearn, E.H.: Predictions of aneurysm formation in distensible tubes: part B–application and comparison of alternative approaches. Int. J. Mech. Sci. **70**, 155–170 (2013)
10. David, G., Humphrey, J.D.: Further evidence for the dynamic stability of intracranial saccular aneurysms. J. Biomech. **36**, 1143–1150 (2003)
11. Gonçalves, P.B., Soares, R.M., Pamplona, D.: Nonlinear vibrations of a radially stretched circular hyperelastic membrane. J. Sound Vib. **327**, 231–248 (2009)
12. Haddow, J.B., Mioduchowski, A.: Dynamic expansion of a compressible hyperelastic spherical shell. Acta Mech. **26**, 179–187 (1977)
13. Haddow, J.B., Lorimer, S.A., Tait, R.J.: Nonlinear axial shear wave propagation in a hyperelastic incompressible solid. Acta Mech. **66**, 205–216 (1987)
14. Haddow, J.B., Lorimer, S.A., Tait, R.J.: Nonlinear combined axial and torsional shear wave propagation in an incompressible hyperelastic solid. Acta Mech. **22**, 297–306 (1987)
15. Janele, P., Haddow, J.B., Mioduchowski, A.: Finite dynamic expansion of a hyperelastic circular cylindrical tube. In: Graham, G.A.C., Malik, S.K. (eds.) Continuum Mechanics and Its Applications, pp. 81–91. Hemisphere Publishing Corporation, Washington (1989)
16. Janele, P., Haddow, J.B., Mioduchowski, A.: Finite amplitude spherically symmetric wave propagation in a compressible hyperelastic solid. Acta Mech. **79**, 25–41 (1989)
17. Janele, P., Mioduchowski, A., Haddow, J.B.: A note on finite dynamic deformation of concentric cylinders. Int. J. Eng. Sci. **29**, 1585–1592 (1991)
18. Knowles, J.K.: Large amplitude oscillations of a tube of incompressible elastic material. Q. Appl. Math. **18**, 71–77 (1960)
19. Knowles, J.K.: On a class of oscillations in the finite deformation theory of elasticity. J. Appl. Mech. **29**, 283–286 (1962)
20. MacCormack, R.W.: The effect of viscosity in hypervelocity impact cratering. Am. Inst. Aeronaut. Astronaut. J. **40**, 69–354 (1969)
21. Mendez-Nuñez, L.R., Carroll, J.J.: Comparison of leapfrog, Smolarkiewicz, and MacCormack schemes applied to nonlinear equations. Mon. Weather Rev. **121**, 565–566 (1993)
22. Mockensturm, E.M., Goulbourne, N.: Dynamic response of dielectric elastomers. Int. J. Non-Linear Mech. **41**, 388–395 (2006)
23. Nowinski, J.L., Wang, A.S.D.: Galerkin's solution to a severely non-linear problem of finite elastodynamics. Int. J. Non-Linear Mech. **1**, 219–228 (1966)
24. Ogden, R.W.: Large deformation isotropic elasticity: on the correlation of theory and experiment for compressible rubberlike solids. Proc. R. Soc. Lond. A Math. Phys. Eng. Sci. **328**, 567–583 (1972)
25. Ogden, R.W.: Non-Linear Elastic Deformations. Dover Publications, Mineola (1997)
26. Rodríguez-Martínez, J.A., Fernández-Sáez, J., Zaera, R.: The role of constitutive relation in the stability of hyper-elastic spherical membranes subjected to dynamic inflation. Int. J. Eng. Sci. **93**, 31–45 (2015)
27. Shah, A.D., Humphrey, J.D.: Finite strain elastodynamics of saccular aneurysms. J. Biomech. **32**, 593–599 (1999)
28. Shahinpoor, M.: Large amplitude oscillations of a hollow spherical dielectric. Int. J. Non-Linear Mech. **7**, 527–534 (1972)
29. Treloar, L.R.G.: Stress-strain data for vulcanised rubber under various types of deformation. Trans. Faraday Soc. **40**, 59–70 (1944)
30. Zhong-Heng, G., Soleki, R.: Free and forced finite-amplitude oscillations of an elastic thick-walled hollow sphere made of incompressible material. Arch. Mech. Stosow. **15**, 427–433 (1963)
31. Zukas, J.A., Scheffer, D.R.: Practical aspects of numerical simulations of dynamic events: effects of meshing. Int. J. Impact Eng. **24**, 925–945 (2000)